

# Elsevier instructions for the preparation of a 2-column format camera-ready paper in L<sup>A</sup>T<sub>E</sub>X

P. de Groot<sup>a\*</sup> and X.-Y. Wang<sup>b</sup>

<sup>a</sup>Mathematics and Computer Science Division, Elsevier Science Publishers B.V.,  
P.O. Box 103, 1000 AC Amsterdam, The Netherlands

<sup>b</sup>Economics Department, University of Winchester,  
2 Finch Road, Winchester, Hampshire P3L T19, United Kingdom

These pages provide you with an example of the layout and style for 100% reproduction which we wish you to adopt during the preparation of your paper. This is the output from the L<sup>A</sup>T<sub>E</sub>X document style you requested.

## 1. FORMAT

Text should be produced within the dimensions shown on these pages: each column 7.5 cm wide with 1 cm middle margin, total width of 16 cm and a maximum length of 20.2 cm on first pages and 21 cm on second and following pages. The L<sup>A</sup>T<sub>E</sub>X document style uses the maximal stipulated length apart from the following two exceptions (i) L<sup>A</sup>T<sub>E</sub>X does not begin a new section directly at the bottom of a page, but transfers the heading to the top of the next page; (ii) L<sup>A</sup>T<sub>E</sub>X never (well, hardly ever) exceeds the length of the text area in order to complete a section of text or a paragraph.

### 1.1. Spacing

We normally recommend the use of 1.0 (single) line spacing. However, when typing complicated mathematical text L<sup>A</sup>T<sub>E</sub>X automatically increases the space between text lines in order to prevent sub- and superscript fonts overlapping one another and making your printed matter illegible.

### 1.2. Fonts

These instructions have been produced using a 10 point Computer Modern Roman. Other recommended fonts are 10 point Times Roman,

---

\*Footnotes should appear on the first page only to indicate your present address (if different from your normal address), research grant, sponsoring agency, etc. These are obtained with the `\thanks` command.

New Century Schoolbook, Bookman Light and Palatino.

## 2. PRINTOUT

The most suitable printer is a laser printer. A dot matrix printer should only be used if it possesses an 18 or 24 pin printhead ("letter-quality").

The printout submitted should be an original; a photocopy is not acceptable. Please make use of good quality plain white A4 (or US Letter) paper size. *The dimensions shown here should be strictly adhered to: do not make changes to these dimensions, which are determined by the document style.* The document style leaves at least 3 cm at the top of the page before the head, which contains the page number.

Printers sometimes produce text which contains light and dark streaks, or has considerable lighting variation either between left-hand and right-hand margins or between text heads and bottoms. To achieve optimal reproduction quality, the contrast of text lettering must be uniform, sharp and dark over the whole page and throughout the article.

If corrections are made to the text, print completely new replacement pages. The contrast on these pages should be consistent with the rest of the paper as should text dimensions and font sizes.

Table 1  
Biologically treated effluents (mg/l)

	Pilot plant		Full scale plant	
	Influent	Effluent	Influent	Effluent
Total cyanide	6.5	0.35	2.0	0.30
Method-C cyanide	4.1	0.05		0.02
Thiocyanide	60.0	1.0	50.0	< 0.10
Ammonia	6.0	0.50		0.10
Copper	1.0	0.04	1.0	0.05
Suspended solids				< 10.0

Reprinted from: G.M. Ritcey, Tailings Management, Elsevier, Amsterdam, 1989, p. 635.

### 3. TABLES AND ILLUSTRATIONS

Tables should be made with L<sup>A</sup>T<sub>E</sub>X; illustrations should be originals or sharp prints. They should be arranged throughout the text and preferably be included *on the same page as they are first discussed*. They should have a self-contained caption and be positioned in flush-left alignment with the text margin within the column. If they do not fit into one column they may be placed across both columns (using `\begin{table*}` or `\begin{figure*}`) so that they appear at the top of a page).

#### 3.1. Tables

Tables should be presented in the form shown in Table 1. Their layout should be consistent throughout.

Horizontal lines should be placed above and below table headings, above the subheadings and at the end of the table above any notes. Vertical lines should be avoided.

If a table is too long to fit onto one page, the table number and headings should be repeated above the continuation of the table. For this you have to reset the table counter with `\addtocounter{table}{-1}`. Alternatively, the table can be turned by 90° ('landscape mode') and spread over two consecutive pages (first an even-numbered, then an odd-numbered one) created by means of `\begin{table}[h]` without a caption. To do this, you prepare the table as a separate L<sup>A</sup>T<sub>E</sub>X document and attach the tables to the empty pages with a few spots of suitable glue.

#### 3.2. Line drawings

Line drawings should be drawn in India ink on tracing paper with the aid of a stencil or should be glossy prints of the same; computer prepared drawings are also acceptable. They should be attached to your manuscript page, correctly aligned, using suitable glue and *not transparent tape*. When placing a figure at the top of a page, the top of the figure should be at the same level as the bottom of the first text line.

All notations and lettering should be no less than 2mm high. The use of heavy black, bold lettering should be avoided as this will look unpleasantly dark when printed.

#### 3.3. Black and white photographs

Photographs must always be sharp originals (*not screened versions*) and rich in contrast. They will undergo the same reduction as the text and should be pasted on your page in the same way as line drawings.

#### 3.4. Colour photographs

Sharp originals (*not transparencies or slides*) should be submitted close to the size expected in publication. Charges for the processing and printing of colour will be passed on to the author(s) of the paper. As costs involved are per page, care should be taken in the selection of size and shape so that two or more illustrations may be fitted together on one page. Please contact the Technical Editor in the Camera-Ready Publications Department at Elsevier for a price quotation and layout instructions before producing your paper in its final form.

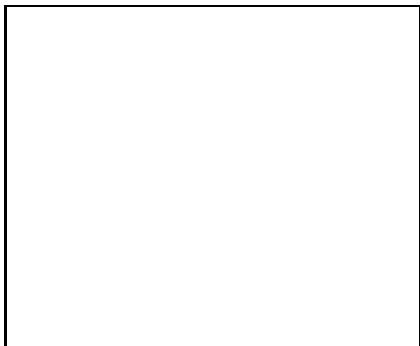


Figure 1. Good sharp prints should be used and not (distorted) photocopies.



Figure 2. Remember to keep details clear and large enough.

#### 4. EQUATIONS

Equations should be flush-left with the text margin;  $\text{\LaTeX}$  ensures that the equation is preceded and followed by one line of white space.  $\text{\LaTeX}$  provides the document-style option `fleqn` to get the flush-left effect.

$$H_{\alpha\beta}(\omega) = E_{\alpha}^{(0)}(\omega)\delta_{\alpha\beta} + \langle \alpha | W_{\pi} | \beta \rangle \quad (1)$$

You need not put in equation numbers, since this is taken care of automatically. The equation numbers are always consecutive and are printed

in parentheses flush with the right-hand margin of the text and level with the last line of the equation. For multi-line equations, use the `eqnarray` environment. For complex mathematics, use the  $\text{\AMSTeX}$  package.

#### REFERENCES

1. S. Scholes, Discuss. Faraday Soc. No. 50 (1970) 222.
2. O.V. Mazurin and E.A. Porai-Koshits (eds.), Phase Separation in Glass, North-Holland, Amsterdam, 1984.
3. Y. Dimitriev and E. Kashchieva, J. Mater. Sci. 10 (1975) 1419.
4. D.L. Eaton, Porous Glass Support Material, US Patent No. 3 904 422 (1975).

References should be collected at the end of your paper. Do not begin them on a new page unless this is absolutely necessary. They should be prepared according to the sequential numeric system making sure that all material mentioned is generally available to the reader. Use `\cite` to refer to the entries in the bibliography so that your accumulated list corresponds to the citations made in the text body.

Above we have listed some references according to the sequential numeric system [1–4].

# Vector and Axial-Vector Spectral Functions and QCD

Andreas Höcker <sup>aa</sup>,

<sup>aa</sup>Laboratoire de l'Accélérateur Linéaire,  
IN2P3-CNRS et Université de Paris-Sud, F-91405 Orsay, France

We present new results for the  $\tau$  hadronic spectral functions analysis using data accumulated by the ALEPH detector at LEP during the years 1991–94. In addition to the vector spectral function, the axial-vector spectral function and, separately, the  $\tau^- \rightarrow 2\pi^- \pi^+ \nu_\tau$  as well as the  $\tau^- \rightarrow \pi^- 2\pi^0 \nu_\tau$  spectral functions are determined from their respective unfolded, *i.e.*, physical invariant mass spectra. The spectral functions are applied to QCD chiral sum rules in order to extract information about saturation at the  $\tau$  mass scale. Using the the semi-leptonic  $\tau$  decay rate for vector and axial-vector currents in addition to spectral moments, we obtain precise measurements of the strong coupling constant  $\alpha_s(M_\tau)$  and the contributing non-perturbative power terms. The evolution to the  $Z$  mass yields  $\alpha_s(M_Z) = 0.1219 \pm 0.0019$ .

## 1. INTRODUCTION

Spectral functions of hadronic  $\tau$  decays are the key objects for various interesting studies concerning resonance structure analysis, the *Conserved Vector Current* hypothesis (CVC) and QCD tests involving strong sum rules and the measurement of  $\alpha_s$ . The ALEPH measurement of the vector spectral functions and related topics was presented at the same conference by R. Alemany [1] (see also [2]).

In this article we deal with new data of the spectral functions from non-strange, axial-vector hadronic  $\tau$  decays measured by the ALEPH Collaboration. We create the sum and the difference of vector and axial-vector spectral functions to get access to information about the saturation of QCD sum rules at the  $\tau$  mass scale. As an application, we determine the electric polarisability of the pion from chiral QCD constraints. In calculating the semi-leptonic  $\tau$  widths and so-called spectral moments of the vector and axial-vector currents, we independently fit the strong coupling constant  $\alpha_s(M_\tau)$  and the respective non-perturbative contributions of the *Operator Product Expansion* (OPE) power series [3,4] using the framework already exploited in previous analyses [5–7]. We finally perform a combined fit of all components in order to obtain the best value of  $\alpha_s(M_\tau)$ .

## 2. SPECTRAL FUNCTIONS OF VECTOR AND AXIAL-VECTOR CURRENTS

The measurement of the non-strange  $\tau$  vector (axial-vector) current spectral functions requires the selection and identification of  $\tau$  decay modes with a G-parity  $G=+1$  ( $G=-1$ ), *i.e.*, hadronic channels with an even (odd) number of neutral *or* charged pions. The isovector spectral function  $v_{1,V^-}$  ( $a_{1,A^-}$ ) of a vector (axial-vector)  $\tau$  decay channel  $V^- \nu_\tau$  ( $A^- \nu_\tau$ ) is obtained by dividing the normalized invariant mass-squared distribution  $(1/N_{V/A^-})(dN_{V/A^-}/ds)$  for a given hadronic mass  $\sqrt{s}$  by the appropriate kinematic factor (throughout this article, charge conjugate states are implied):

$$v_{1,V^-}/a_{1,A^-}(s) = \frac{M_\tau^2}{6 |V_{ud}|^2 S_{EW}} \frac{B(\tau^- \rightarrow V/A^- \nu_\tau)}{B(\tau^- \rightarrow e^- \nu_\tau \bar{\nu}_e)} \times \frac{dN_{V/A^-}}{N_{V/A^-} ds} \left[ \left(1 - \frac{s}{M_\tau^2}\right)^2 \left(1 + \frac{2s}{M_\tau^2}\right) \right]^{-1}, \quad (1)$$

where  $|V_{ud}| = 0.9752 \pm 0.0007$  denotes the CKM weak mixing matrix element [8] and  $S_{EW} = 1.0194$  accounts for electroweak second order corrections [9]. The  $\tau$  mass  $M_\tau = 1776.96^{+0.31}_{-0.27}$  MeV/ $c^2$  is taken from the recent BES measurement [10]. The spectral

functions are normalized by the ratio of the respective vector/axial-vector branching fraction  $B(\tau^- \rightarrow V^-/A^- \nu_\tau)$  to the branching fraction of the electron channel  $B(\tau^- \rightarrow e^- \bar{\nu}_e \nu_\tau) = 17.79 \pm 0.04$  [11], where the latter is additionally constrained via universality from  $B(\tau^- \rightarrow \mu^- \bar{\nu}_\mu \nu_\tau)$  and the  $\tau$  lifetime. Note that our definition of the  $\tau$  spectral functions differs from the one used in [12] by an additional factor  $4\pi^2$ .

Assuming unitarity (which implies the *optical theorem*) and analyticity to hold, the spectral functions of hadronic  $\tau$  decays are related via dispersion relations to the imaginary parts of the two-point correlation functions  $\Pi_{ij,U}^{\mu\nu}(q) = i \int d^4x e^{iqx} \langle 0 | T(U_{ij}^\mu(x) U_{ij}^\nu(0)^\dagger) | 0 \rangle$  of vector ( $U \equiv V = \bar{\psi}_j \gamma^\mu \psi_i$ ) or axial-vector ( $U \equiv A = \bar{\psi}_j \gamma^\mu \gamma_5 \psi_i$ ) colour-singlet quark currents in corresponding quantum states (see, *e.g.*, [4,13]).

### 3. THE MEASUREMENT PROCEDURE

The measurement of the spectral functions defined in Eq. (1) requires the determination of the physical invariant mass-squared distribution. The details of the analysis are reported in [2]. A description of the ALEPH detector and its performance is published in [14].

In the following, we will briefly outline the important steps of the measurement procedure:

- **Tau pairs** originating from  $Z^0$  decays are detected utilizing their characteristic collinear jet signature and the low multiplicity of their decays. Using the data from 1991–94, a total 124 358  $\tau$  pairs is selected corresponding to a detection efficiency of  $(78.8 \pm 0.1)\%$ . The overall non- $\tau$  background contribution in the hadronic modes amounts to  $(0.6 \pm 0.2)\%$ . Details about the ALEPH  $\tau$  pair selection are given in [16–18].

- **Charged particles** (electrons, muons and hadrons) are identified employing a maximum likelihood method to combine different and essentially uncorrelated information measured for each individual track. The procedure and the discriminating variables used in this analysis are described in [19,17]. The calibration of charged

tracks is performed using low radiating  $e^+e^- \rightarrow \mu^+\mu^-$  events at beam energy and the invariant mass measurement of well-known, narrow resonances at low and intermediate energies. The resulting calibration uncertainty amounts to less than 0.1%.

- **Photons** are reconstructed by collecting associated energetic electromagnetic calorimeter (ECAL) towers, forming a *cluster*. To distinguish genuine photons from fake photons a likelihood method is applied using ECAL information, *e.g.*, the fraction of energy in the respective ECAL stacks, the transverse size of the shower or the distance between the barycentre of the cluster and the closest charged track. The energy calibration is performed using electrons originating from Bhabha,  $\tau$  and two-photon events. We obtain a relative calibration uncertainty of about 1.5% at low energy, 1% at intermediate energies and 0.5% at high energy.

- The  **$\pi^0$  finder** uses the virtue of a  $\pi^0$ -mass constraint fit to correctly attribute two reconstructed photons to the corresponding  $\pi^0$  decay. At higher  $\pi^0$  energy, the opening angle between the boosted photons tends to become smaller than the calorimeter resolution so that the two electromagnetic showers are often merged in one cluster. The transverse energy distribution in the ECAL nevertheless allows the computation of energy-weighted moments providing a measure of the two-photon invariant mass. Remaining photons are considered as originating from a  $\pi^0$  where the second photon has been lost.

- The **classification** of the inclusive hadronic  $\tau$  decay channels is performed according to [18] on the basis of the number of reconstructed charged and neutral pions. The exclusive channels listed in Table 1 are obtained by subtracting the  $\tau$  and non- $\tau$  background and the strange contribution from the inclusive measurements using the Monte Carlo simulation. In order to extract the physical invariant mass spectra from the measured ones it needs to be *unfolded* from the effects of measurement distortion.

- The **unfolding method** used here is based

Table 1

Vector and axial-vector hadronic  $\tau$  decay modes with their contributing branching fractions. According to [15], the  $K\bar{K}\pi$  channels are assumed to be  $(78_{-28}^{+22})\%$  vector and  $(25 \pm 25)\%$  axial-vector, while the errors are 100% anti-correlated. The  $K\bar{K}\pi\pi\nu_\tau$  modes are conservatively assumed to have  $(50 \pm 50)\%$  vector and axial-vector parts.

Vector	BR (in %)	Axial-Vector	BR (in %)
$\pi^- \pi^0 \nu_\tau$	$25.35 \pm 0.19$	$\pi^-$	$11.23 \pm 0.16$
$\pi^- 3\pi^0 \nu_\tau$	$1.17 \pm 0.14$	$\pi^- 2\pi^0 \nu_\tau$	$9.23 \pm 0.17$
$2\pi^- \pi^+ \pi^0 \nu_\tau$	$2.54 \pm 0.09$	$2\pi^- \pi^+ \nu_\tau$	$9.13 \pm 0.15$
$\pi^- 5\pi^0 \nu_\tau$	} $0.04 \pm 0.02^{(1)}$	$\pi^- 4\pi^0 \nu_\tau$	$0.03 \pm 0.03^{(1)}$
$2\pi^- \pi^+ 3\pi^0 \nu_\tau$		$2\pi^- \pi^+ 2\pi^0 \nu_\tau$	$0.10 \pm 0.02$
$3\pi^- 2\pi^+ \pi^0 \nu_\tau$		$3\pi^- 2\pi^+ \nu_\tau$	$0.08 \pm 0.02$
$\omega \pi^- \nu_\tau^{(2)}$	$1.83 \pm 0.09$	$\omega \pi^- \pi^0 \nu_\tau^{(2)}$	$0.42 \pm 0.09$
$\eta \pi^- \pi^0 \nu_\tau^{(3)}$	$0.17 \pm 0.03$	$\eta 2\pi^- \pi^+ \nu_\tau$	$0.04 \pm 0.01$
–	–	$\eta \pi^- 2\pi^0 \nu_\tau$	$0.02 \pm 0.01$
$K^- K^0 \nu_\tau$	$0.19 \pm 0.04$	–	–
$K^- K^+ \pi^- \nu_\tau$	$0.13 \pm 0.05$	$K^- K^+ \pi^- \nu_\tau$	$0.04 \pm 0.04$
$K^0 \bar{K}^0 \pi^- \nu_\tau$	$0.13 \pm 0.05^{(1)}$	$K^0 \bar{K}^0 \pi^- \nu_\tau$	$0.04 \pm 0.04$
$KK^0 \pi^0 \nu_\tau$	$0.08 \pm 0.04$	$KK^0 \pi^0 \nu_\tau$	$0.03 \pm 0.03$
$KK\pi\pi$	$0.08 \pm 0.08^{(1)}$	$KK\pi\pi$	$0.08 \pm 0.08^{(1)}$
Total Vector	$31.71 \pm 0.31$	Total Axial-Vector	$30.42 \pm 0.32$

<sup>1</sup> The branching ratio is obtained using constraints from isospin symmetry (see text and [2]).

<sup>2</sup> Through  $\omega \rightarrow \pi^- \pi^+ \pi^0$ , 88.8% of this channel is reconstructed in  $2\pi^- \pi^+ \pi^0 \nu_\tau$ .

<sup>3</sup> Through  $\eta \rightarrow 2\gamma$ , 39.3% of this channel is reconstructed in  $\pi^- 3\pi^0 \nu_\tau$ .

on the regularised inversion of the detector response matrix, obtained from the Monte Carlo simulation, using the *Singular Value Composition* technique. Details are published in [20].

### Systematic Errors

The study of systematic errors affecting the measurement is subdivided into several classes according to their origin, *viz.*, the photon and  $\pi^0$  reconstruction, the charged track measurement, the unfolding procedure and additional sources. Since we use an unfolding procedure based upon a detector response matrix from the Monte Carlo simulation, the reliability of the simulation has to be subjected to detailed studies [2,1,18].

In order to check the photon reconstruction in the ECAL, we studied the influence of calibration and resolution uncertainties as well as possible problems with the reference distributions of

a likelihood used to veto fake photon candidates, of the contamination and energy distribution of fake photons, of the photon detection efficiency at threshold energies ( $E_\gamma^{\text{thresh}} = 300$  MeV) and in the neighborhood of charged tracks.

Correspondingly, the effects of calibration and resolution uncertainties in the measurement of charged tracks are checked, accompanied by tests of the reconstruction efficiency of highly collimated multi-prong events, and the simulation of secondary nuclear interactions.

In addition, systematic errors introduced by the unfolding procedure are tested by comparing known, true distributions to their respective unfolded ones and by varying the regularisation conditions.

Finally, we add systematic errors due to the limited Monte Carlo statistics and to uncertainties in the branching ratios of the respective  $\tau$  decay modes.

## Invariant Mass Spectra and Spectral Functions

The measurement procedure sketched above provides the physical invariant mass spectra of the measured  $\tau$  decay modes including their respective bin-to-bin covariance matrices obtained after the unfolding of the spectra from the statistical errors and the study of systematic uncertainties.

The exclusive vector and axial-vector  $\tau$  decay channels are listed in Table 1. The branching ratios shown are mainly taken from [18], including recent improvements in the precision of the measurements of  $\tau$  decays involving  $\eta$  and  $\omega$  mesons [21,22] as well as Kaons [23].

The total vector and axial-vector current spectral function (1) is obtained by summing up the exclusive spectral functions with the addition of small contributions from unmeasured modes. These are taken from the KORALZ3.8, TAUOLA1.5 [24]  $\tau$  Monte Carlo simulation (accompanied by an inflated systematic error), as discussed below.

### Vector Spectral Function

The two- and four-pion states are measured exclusively, while the six-pion state is only partly measured. The total six-pion branching ratio has been determined in [2] using isospin symmetry. However, this procedure is not straight forward, as one has to consider that the six-pion channel is contaminated by isospin-violating  $\tau^- \rightarrow \eta 2\pi^- \pi^+$ ,  $\eta \pi^- 2\pi^0 \nu_\tau$  decays (which were reported for the first time by the CLEO Collaboration [22]).

The small fraction of the  $\omega \pi^- \nu_\tau$  decay channel that is not reconstructed in the four-pion final state is added using the simulation.

Similarly, we correct for  $\eta \pi^- \pi^0 \nu_\tau$  decay modes other than  $\eta \rightarrow 2\gamma$  which is classified in the  $h^- 3\pi^0 \nu_\tau$  final state.

The  $K^- K^0 \nu_\tau$  is taken entirely from the simulation.

Using isospin constraints from  $\tau$  branching ratios deduced in [25], it can be shown [15] that the  $K\bar{K}\pi$  channels are  $(78^{+22}_{-28})\%$  vector. The corresponding spectral functions are obtained from the Monte Carlo simulation.

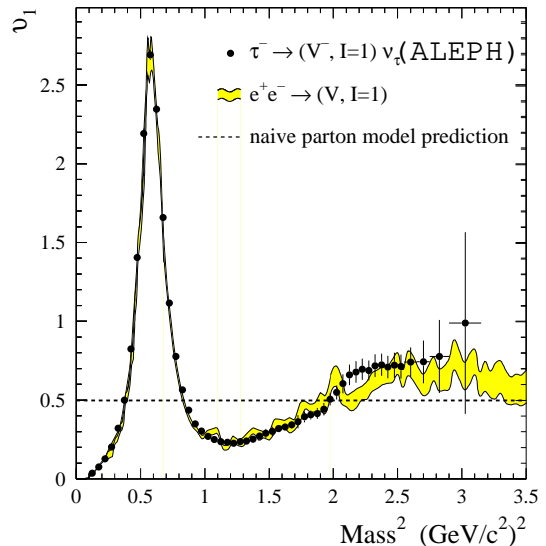


Figure 1. Total  $\tau$  vector current spectral function. The band shows the corresponding  $e^+e^-$  annihilation data obtained from isovector final states translated to  $\tau$  decays via isospin rotation as comprehensively explained in [2]. The dashed line represents the naive parton model prediction, while the QCD corrected prediction lies roughly 20% higher.

A preliminary ALEPH analysis [2] of  $\tau$  decays into  $K\bar{K}\pi\pi$  final states yields a total branching ratio of  $(0.17 \pm 0.05)\%$ . However, their vector and axial-vector parts are unknown and are therefore both estimated to be  $(50 \pm 50)\%$ .

For additional details on the vector spectral functions see Ref. [2,1]. The total  $\tau$  vector spectral function is compared to the isospin rotated cross sections from isovector  $e^+e^-$  final states [2,1] is depicted in Fig. 1. The agreement between both curves is fairly good, keeping in mind the appearance of large bin-to-bin correlations within the  $\tau$  spectral function as a consequence of the necessary regularisation during the unfolding procedure.

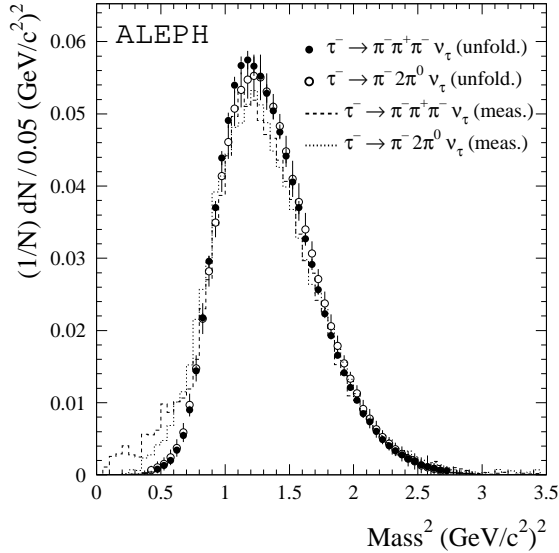


Figure 2. Unfolded (physical) invariant mass-squared spectra of the  $\tau$  final states  $2\pi^-\pi^+\nu_\tau$  and  $\pi^-2\pi^0\nu_\tau$ . The dashed/dotted line shows the corresponding measured distribution.

### Axial-Vector Spectral Function

The three-pion spectral functions are measured in both occurring final states. Fig. 2 shows the unfolded  $2\pi^-\pi^+\nu_\tau$  and  $\pi^-2\pi^0\nu_\tau$  mass spectra with reasonable agreement in form and normalization. The small bump of the measured  $2\pi^-\pi^+\nu_\tau$  spectrum at low mass (Fig. 2) is caused by decays where only two charged tracks are reconstructed. Due to incomplete ECAL energy collection, the measured  $\pi^-2\pi^0\nu_\tau$  distribution is slightly shifted to lower masses. These details are well reproduced by the Monte Carlo simulation. We assume in the following that both channels have identical spectra and use the weighted average of the distributions for the total axial-vector spectral function.

The five-pion spectral functions are exclusively measured in the  $2\pi^-\pi^+2\pi^0\nu_\tau$  and  $3\pi^-2\pi^+\nu_\tau$  final states. Using Pais' isospin classes [26], the branching fraction of  $\pi^-4\pi^0\nu_\tau$  can be bounded entirely using the  $3\pi^-2\pi^+\pi^0\nu_\tau$  branching fraction. It is found to be smaller than 0.055%. We

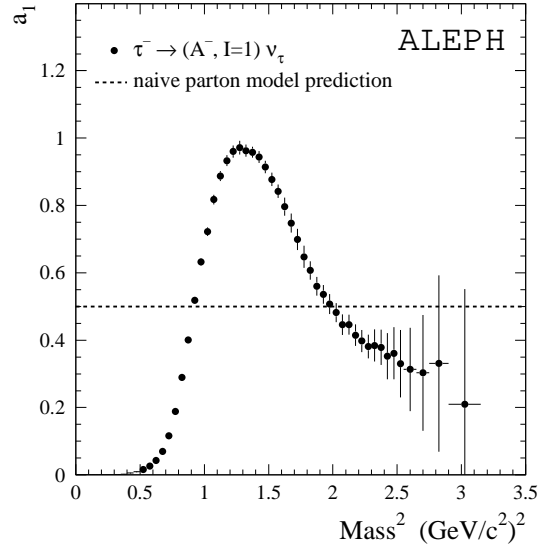


Figure 3. Total  $\tau$  axial-vector current spectral function. The dashed line represents the naive parton model prediction, while the QCD-corrected prediction lies roughly 20% higher.

take half of this upper limit with an error of 100%.

In analogy to the vector case, we add the small fraction of the  $\omega\pi^-\pi^0\nu_\tau$  decay channel that is not accumulated in the  $2\pi^-\pi^+2\pi^0\nu_\tau$  final state using the simulation.

Also considered are the axial-vector  $\eta(3\pi)^-\nu_\tau$  final states [22] and, as in the vector case, a  $(50 \pm 50)\%$   $K\bar{K}\pi\pi\nu_\tau$  contribution. Both spectral functions are taken from the simulation accompanied by comfortable systematic errors due to the uncertainty of the respective invariant mass distributions.

The total axial-vector spectral function is plotted in Fig. 3. However, we are still not in the asymptotic region at the  $\tau$  mass scale. We may expect additional oscillations to lift the spectral function to roughly 1.2 times the naive parton model prediction (that is expected asymptotically).

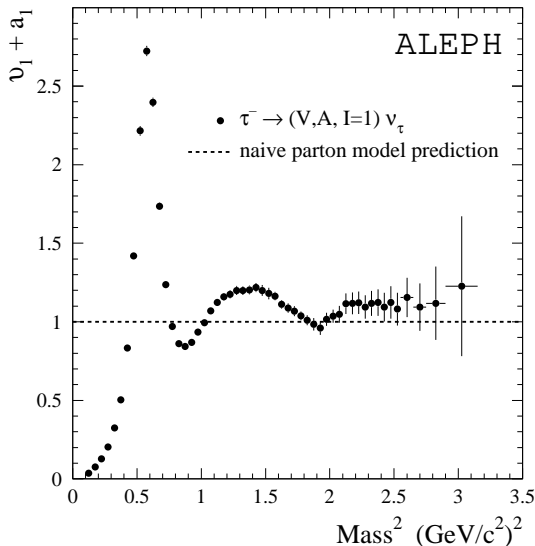


Figure 4. Inclusively measured vector plus axial-vector ( $v_1 + a_1$ ) spectral function. Again, the dashed line represents the naive parton model prediction.

### $(v_1 + a_1)$ Spectral Function

In the favourable case of the vector plus axial-vector spectral function we do not have to distinguish the current properties of the respective non-strange hadronic  $\tau$  decay channels. Hence we measure the mixture of all contributing non-strange final states as inclusively as possible. The dominating two- and three-pion final states are still measured exclusively, while the remaining contributing topologies are treated inclusively, *i.e.*, without any subtraction of  $\tau$ -background originating from one of the considered decay modes. This improves the statistical error. Another advantage is, that we do not have to worry about the current properties of the  $K\bar{K}\pi$  and  $K\bar{K}\pi\pi$  modes or about possible missing, *i.e.*, unmeasured,  $\tau$  decay modes as they are necessarily contained in the inclusive sample.

The  $(v_1 + a_1)$  spectral function is depicted in Fig. 4. The improvement in precision in comparison to an exclusive sum of Fig. 1 and Fig. 3

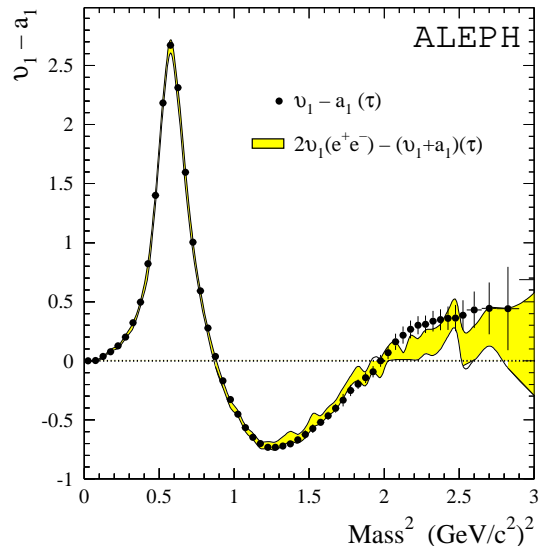


Figure 5. Vector minus axial-vector ( $v_1 - a_1$ ) spectral function. The band shows the corresponding spectral function using two times the vector spectral function from  $e^+e^-$  annihilation data minus the inclusively measured  $(v_1 + a_1)$  spectral function from  $\tau$  decays.

becomes obvious at higher mass-squared. One clearly sees the oscillating spectral function which does not seem to approach the asymptotic limit at  $s \rightarrow M_\tau^2$ , which is predicted from perturbative QCD to lie about 20% higher than the naive parton model prediction.

## 4. QCD CHIRAL SUM RULES

As important application of the results obtained from the spectral function analysis above, we present a study of four QCD sum rules involving the difference of the vector and the axial-vector spectral functions, each deduced from vector and axial-vector current conservation in the limit of the chiral symmetry ( $m_u = m_d = 0$ ,

$m_\pi = 0$ )<sup>1</sup>:

$$\frac{1}{4\pi^2} \int_0^{s_0 \rightarrow \infty} ds \frac{v_1(s) - a_1(s)}{s} = f_\pi^2 \frac{\langle r_\pi^2 \rangle}{3} - F_A, \quad (2)$$

$$\frac{1}{4\pi^2} \int_0^{s_0 \rightarrow \infty} ds (v_1(s) - a_1(s)) = f_\pi^2, \quad (3)$$

$$\frac{1}{4\pi^2} \int_0^{s_0 \rightarrow \infty} ds s (v_1(s) - a_1(s)) = 0, \quad (4)$$

$$\frac{1}{4\pi^2} \int_0^{s_0 \rightarrow \infty} ds s \ln \frac{s}{\Lambda^2} (v_1(s) - a_1(s)) = -\frac{16\pi^2 f_\pi^2}{3\alpha} (m_{\pi^\pm}^2 - m_{\pi^0}^2). \quad (5)$$

Eq. (2) is known as the Das-Mathur-Okubo (DMO) sum rule [27]. It relates the given integral ( $I_{\text{DMO}}$ ) to the square of the pion decay constant<sup>2</sup>  $f_\pi = (92.4 \pm 0.26)$  MeV [8] obtained from the decays  $\pi^- \rightarrow \mu^- \bar{\nu}_\mu$  and  $\pi^- \rightarrow \mu^- \bar{\nu}_\mu \gamma$ ; to the pion axial-vector form factor  $F_A$  for radiative decays  $\pi^- \rightarrow \ell^- \bar{\nu}_\ell \gamma$ ; and to the pion charge radius-squared  $\langle r_\pi^2 \rangle = (0.431 \pm 0.026)$  fm<sup>2</sup> [29], determined by means of a careful fit to space-like data [28] using a two-loop chiral expansion coefficient as additional degree of freedom. The error of  $\langle r_\pi^2 \rangle$  includes theoretical uncertainties. For completeness we will also express the results on the pion polarisability (see next paragraph) in terms of the standard value  $\langle r_\pi^2 \rangle = (0.439 \pm 0.008)$  fm<sup>2</sup> [28] obtained from a one parameter fit to the same data [28]. Eqs (3) and (4) are the first and second Weinberg sum rules (WSR) [30], where the pion pole in (3) is already integrated out. When switching quark masses on, only the first WSR remains valid while the second WSR breaks down due to contributions from the difference of non-conserved vector and axial-vector currents of order  $m_q^2/s$ , leading to a quadratic divergence of the integral [31].

<sup>1</sup> We now identify the vector and axial-vector spectral functions with the absorptive parts of the corresponding two-point correlation functions  $\Pi_{ij,V/A}^{\mu\nu}$ .

<sup>2</sup> Our definition of  $f_\pi$  differs from the one used in [8] by a factor of  $\sqrt{2}$ .

Finally, Eq. (5) represents the electromagnetic splitting of the pion masses [32].

Fig. 5 shows the vector minus axial-vector distribution obtained from  $\tau$  decays in addition to two times the vector spectral function from  $e^+e^-$  annihilation data minus the inclusive  $(v_1 + a_1)$  measurement, yielding a corresponding  $(v_1 - a_1)$  spectral function with a slightly better precision at the end of the  $\tau$  phase space. The sum rules (2)–(5) versus the upper integration bound  $s_0 \leq M_\tau^2$  are plotted in Figs. 6a–d. In addition to the  $\tau$  spectral functions, we again show the contribution from  $e^+e^-$  annihilation combined with the  $(v_1 + a_1)$  inclusive measurement. The horizontal band depicts the corresponding chiral prediction of the integrals taken from [12].

We stress that only for the DMO sum rule (Fig. 6a), where contributions from higher mass-squares are suppressed, does the saturation within the one sigma error seem to occur at the  $\tau$  mass scale. The other sum rules (Fig. 6b–c) are apparently not saturated at  $M_\tau^2$  as already indicated by the non-vanishing  $(v_1 - a_1)$  spectral function at the end of the  $\tau$  phase space. This is due to a small axial-vector contribution that is clearly below the QCD prediction at  $M_\tau^2$  as can be seen in Fig. 3.

## The Polarisability of the Pion

In order to quantify the actual precision of the sum rules above, we determine the electric polarisability<sup>3</sup> of the pion, given by [33]

$$\alpha_E = \frac{\alpha F_A}{m_\pi f_\pi^2}, \quad (6)$$

utilizing the DMO sum rule  $I_{\text{DMO}}$  (2) as proposed in [34]. The computation of the pion axial-vector form factor  $F_A$  is most accurate using the measurement of the ratio  $\gamma \equiv F_A/F_V$  obtained from radiative pion decays  $\pi^- \rightarrow e^- \bar{\nu}_e \gamma$ . Using the weighted average  $\gamma = 0.46 \pm 0.05$  of the measurements [35]

<sup>3</sup> The electric polarisability  $\alpha_E$  of a physical system can be understood classically as the proportionality constant which governs the induction of the dipole moment  $\mathbf{p}$  of a system in the presence of an external electric field  $\mathbf{E}$ :  $\mathbf{p} = \alpha_E \mathbf{E}$ . The polarisability is an important quantity to characterize a particle, *i.e.*, in probing its inner structure.

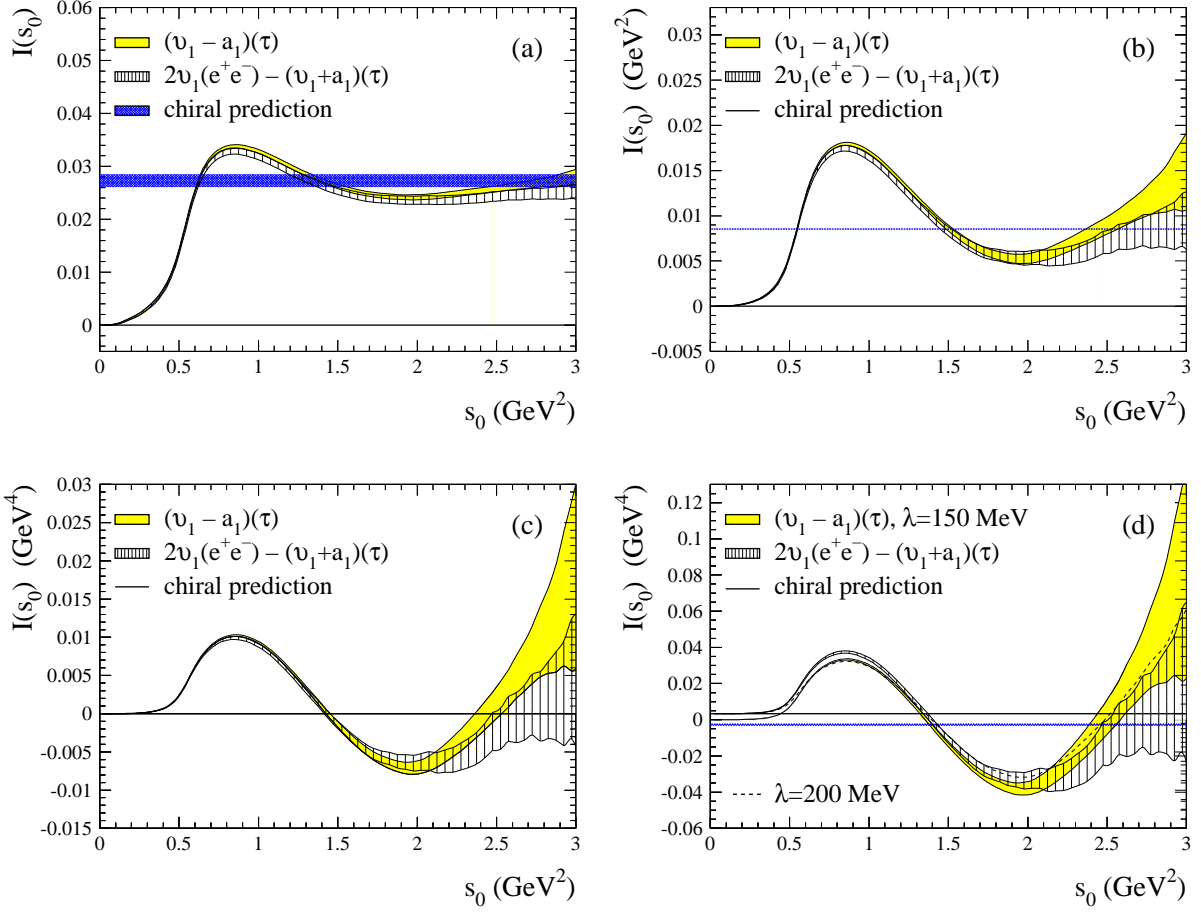


Figure 6. Sum rules corresponding to Eqs (2)–(5) (plots: a–d) versus the upper integration bound  $s_0$ .

as well as the CVC relation between the pion vector form factor and the  $\pi^0$  lifetime  $|F_V| = (1/\alpha)(2\pi\tau_{\pi^0}m_{\pi^0})^{-1/2} = 0.0132 \pm 0.0005$  [36,8], we have

$$\alpha_E^{\text{theo}} = (2.86 \pm 0.33) \times 10^{-4} \text{ fm}^3 \quad (7)$$

as a theoretical prediction.

Using the  $\tau$  ( $v_1 - a_1$ ) spectral functions, we evaluate the DMO integral at the  $\tau$  mass scale as  $I_{\text{DMO}}^\tau = (28.0 \pm 1.6 \pm 1.1) \times 10^{-3}$ , where the first error is the direct propagated integration error using the covariance matrices of the spectral functions. The second error accounts for interpolation biases that occur because we do not integrate up to exactly  $s_0 = M_\tau^2$  since

the error of the spectral function diverges at the very end of the  $\tau$  phase space. For the  $2v_1(e^+e^-) - (v_1 + a_1)(\tau)$  spectral function we obtain  $I_{\text{DMO}}^{\tau, e^+e^-} = (25.2 \pm 1.3 \pm 0.4) \times 10^{-3}$  with a  $\chi^2 = 2.7/1$  when compared to the above pure  $\tau$  result, assuming both measurements to be 50% correlated. The weighted average (taking into account the correlation) is

$$\langle I_{\text{DMO}} \rangle = (26.4 \pm 1.5) \times 10^{-3}. \quad (8)$$

According to the prescription of Ref. [8], we increased the error by  $\sqrt{\chi^2/1}$  to account for some inconsistency. Combining (2) and (6) with the assumption that the contribution to (2) for  $s_0 > M_\tau^2$  is negligible, *i.e.*, the integral is saturated,

one finds that the pion polarisability is

$$\alpha_E^{\text{exp}} = (2.40 [2.68] \pm 1.14 [0.76]) \times 10^{-4} \text{ fm}^3. \quad (9)$$

The figures in brackets give the corresponding result if we use the standard value of  $\langle r_\pi^2 \rangle = (0.439 \pm 0.008) \text{ fm}^2$  [28] for the pion charge radius-squared. Both results (9) are in agreement with the chiral prediction (7).

The authors of [34] (see also [37]) used the first WSR (3) as an additional constraint to considerably improve the precision and the reliability of the  $I_{\text{DMO}}$  evaluation as it naturally reduces the sensitivity to the saturation assumption.

Another approach to the solution of (2) deals with the Laplace-transformed DMO sum rule, which suppresses the high energy tail of the spectral function in order to improve saturation at  $M_\tau^2$  and to increase the precision of the integral [34,38]:

$$\hat{I}_{\text{DMO}}(M^2) = \frac{1}{4\pi^2} \int_0^{s_0 \rightarrow \infty} ds e^{-s/M^2} \frac{v_1(s) - a_1(s)}{s} + \frac{f_\pi^2}{M^2} - \frac{C_6 \langle \mathcal{O}(6) \rangle}{6M^6} - \frac{C_8 \langle \mathcal{O}(8) \rangle}{24M^8} \quad (10)$$

where  $\hat{I}_{\text{DMO}}(M^2) = I_{\text{DMO}}$  in the limit  $M^2 \rightarrow \infty$ . At sufficiently high  $M^2$  the impact of the dimension  $D = 6$  and dimension  $D = 8$  non-perturbative terms on  $\hat{I}_{\text{DMO}}(M^2)$  is small. One may use projecting sum rules with improved saturation to determine the corresponding phenomenological operators:

$$-4\pi^2 C_6 \langle \mathcal{O}(6) \rangle \simeq \int_0^{s_0} ds s^2 (v_1(s) - a_1(s)) - \beta_1 s_0 \int_0^{s_0} ds s (v_1(s) - a_1(s)), \quad (11)$$

$$4\pi^2 C_8 \langle \mathcal{O}(8) \rangle \simeq \int_0^{s_0} ds s^3 (v_1(s) - a_1(s)) - \beta_2 s_0^2 \int_0^{s_0} ds s (v_1(s) - a_1(s)). \quad (12)$$

Obviously, Eq. (11) and (12) hold for  $s_0 \rightarrow \infty$  since the second term on the r.h.s. vanishes in the chiral limit by virtue of the second WSR (4). Unfortunately, the gain in convergence of the sum rules obtained from the insertion of the (even less convergent) second WSR is not very successful as it is accompanied by large additional errors. The coefficients  $\beta_{1/2}$  in (11) and (12) depend on the high energy tail of the  $(v_1 - a_1)$  spectral function which can be expanded in powers of  $s_0$ . They are estimated to be  $\beta_1 \approx 1.5$  and  $\beta_2 \approx 2.8$ . We obtain, for the non-perturbative contributions, the extremely rough estimates (using  $\tau$  data only):  $C_6 \langle \mathcal{O}(6) \rangle = 0.025 \pm 0.027 \text{ GeV}^6$  and  $C_8 \langle \mathcal{O}(8) \rangle = -0.15 \pm 0.16 \text{ GeV}^8$ . This yields the most precise value of  $\hat{I}_{\text{DMO}} = (26.3 \pm 0.6)$  for  $\tau$  spectral functions at (high)  $M^2 = 2.6 \text{ GeV}^2$  enabling one to avoid the large errors of the inaccurate operator terms at low energy.

A more promising solution of Eq. (10) lies in a simultaneous fit of  $\hat{I}_{\text{DMO}}$  and the non-perturbative terms by means of moments on the Borel parameter  $M^2$ . We perform a  $\chi^2$  fit using the (strongly correlated) moments  $M^2 = 0.2, 0.7, 1.2, \dots, 3.7 \text{ GeV}^2$  in order to guarantee sufficient information for the constraint of the dimension  $D = 6$  and  $D = 8$  operators at low  $M^2$  and non-biased, purely perturbative contributions at high  $M^2$  to fix  $\hat{I}_{\text{DMO}}$  through the Laplace-transformed DMO integral in (10). The fit converges with a  $\chi^2 = 2.3$  over 5 degrees of freedom, yielding (for  $\tau$  data)

$$\hat{I}_{\text{DMO}} = (25.8 \pm 0.3 \pm 0.1) \times 10^{-3}, \quad (13)$$

which is in agreement with (8). The second error accounts for estimated uncertainties induced by the saturation assumption. From the fit, the non-perturbative contributions are  $C_6 \langle \mathcal{O}(6) \rangle = 0.0029 \pm 0.0002 \text{ GeV}^6$  and  $C_8 \langle \mathcal{O}(8) \rangle = -0.0015 \pm 0.0003 \text{ GeV}^8$  with an anti-correlation of nearly 100%.

Fig. 7 depicts  $\hat{I}_{\text{DMO}}$  as a function of  $M^2$  for the pure  $\tau$  and the combined  $\tau$  and  $e^+e^-$  annihilation  $(v_1 - a_1)$  spectral functions. In this case, the pure  $\tau$  spectral function provides smaller errors because of the more accurate two-pion contribution in  $\tau$  decays which is strongly weighted in (10).

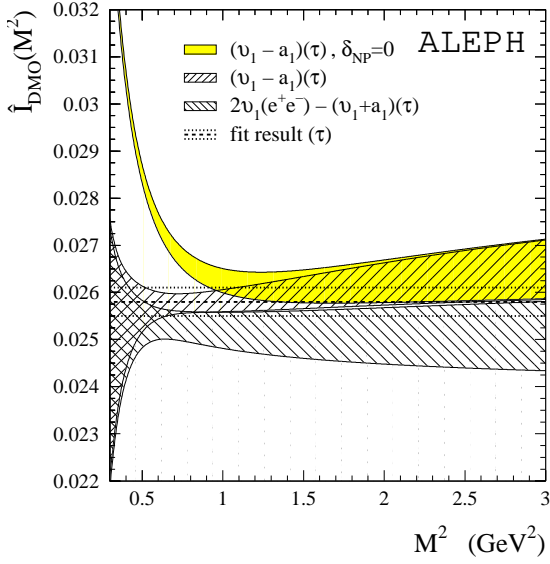


Figure 7. Laplace-transformed DMO sum rule  $\hat{I}_{\text{DMO}}$  as a function of the Borel parameter  $M^2$  for the exclusive  $\tau$  and the combined  $e^+e^-$ ,  $\tau(v_1 - a_1)$  spectral function. The shaded area gives the  $\tau$  integral without the non-perturbative contributions. It diverges hyperbolically at small  $M^2$ .

The shaded band shows the  $\tau$  result without the non-perturbative terms. Non-perturbative contributions dominate the integral at  $M^2 < 1 \text{ GeV}^2$  and become negligible for  $M^2 > 2.5 \text{ GeV}^2$  as the comparison between the shaded and the hatched bands demonstrates.

Using (13) the electric polarisability is

$$\alpha_E^{\text{exp}} = (2.68 [2.96] \pm 0.91 [0.32]) \times 10^{-4} \text{ fm}^3 \quad (14)$$

with significantly lower errors compared to (9) due to the improved convergence of the Laplace-transformed DMO sum rule. Again the figures in brackets give the corresponding result when using the standard value of  $\langle r_\pi^2 \rangle$ .

## 5. THE MEASUREMENT OF $\alpha_s$

Tests of Quantum Chromodynamics and the precise measurement of the strong coupling constant  $\alpha_s$  at the  $\tau$  mass scale carried out for the first time by ALEPH [5,6] and CLEO [7] have

been the subject of engaged discussions about theoretical and experimental implications, accompanied by a considerable number of interesting publications (see, *e.g.*, [39,40,13,41]). Following the spirit of the previous ALEPH analysis [5,6], we determine  $\alpha_s(M_\tau)$  and the contributing non-perturbative terms for the first time using the vector, axial-vector as well as vector plus axial-vector spectral functions and from a combined fit of all substantially uncorrelated input variables.

### The $\tau$ Semileptonic Width

Using the analytic property of the vector/axial-vector two-point correlation functions  $\Pi_{ij,V/A}^{(J)}$ , the non-strange, semileptonic  $\tau$  decay rates  $R_{\tau,V/A}$  can be expressed as contour integrals in the complex  $s$ -plane [42,4]

$$R_{\tau,V/A} = 6\pi i \oint_{|s|=M_\tau^2} \frac{ds}{M_\tau^2} \left(1 - \frac{s}{M_\tau^2}\right)^2 \times \left[ \left(1 + \frac{2s}{M_\tau^2}\right) \Pi_{ud,V/A}^{(0+1)} - \frac{2s}{M_\tau^2} \Pi_{ud,A}^{(0)} \right]. \quad (15)$$

The advantage of this formulation is that it avoids the integration over the whole energy-squared spectrum which includes large, uncontrolled non-perturbative effects.

By means of the short distance OPE, the theoretical prediction of  $R_{\tau,V/A}$  separates in the following contributions

$$R_{\tau,V/A} = \frac{3}{2} |V_{ud}|^2 S_{\text{EW}} (1 + \delta'_{\text{EW}} + \delta_{\text{P}} + \delta_{\text{mass}} + \delta_{\text{NP}}), \quad (16)$$

where  $|V_{ud}| = 0.9752 \pm 0.0007$  [8],  $S_{\text{EW}} = 1.0194$  as in (1) and the small non-logarithmic electroweak correction  $\delta'_{\text{EW}} \simeq 0.0010$  [43].

The perturbative contribution  $\delta_{\text{P}}$  of the correlators in (15) is known to next-to-next-to-leading order  $\alpha_s^3$ . Moreover, the series is resummed to all orders up to the unknown perturbative coefficients of the QCD  $\beta$ -function. Hence the convergence of the series is reinforced and the dependence on the scale and the choice of the renormalization scheme is reduced [40].

The leading quark mass correction  $\delta_{\text{mass}}$  in (16) is safely neglected for  $u$  and  $d$  quarks ( $\approx -0.08\%$  [13]).

For the non-perturbative contribution  $\delta_{\text{NP}}$  we use the SVZ-approach [3] in terms of a power series of  $M_\tau$ . Long-distance QCD effects are thereby separated into unpredictable, non-perturbative contributions, absorbed in dimensional, phenomenological operators  $\mathcal{O}(D)$  and into short distance parts  $C_D$  (Wilson Coefficients), calculable within perturbative QCD:

$$\delta_{\text{NP}} = \sum_{D=4,6,8} \delta^{(D)} = \sum_{D=4,6,8} C_D \frac{\mathcal{O}(D)}{(-M_\tau^2)^{D/2}}. \quad (17)$$

The first operator that involves non-perturbative physics appears at  $D = 4$  and is linked to the gluon condensate.

### Spectral Moments

To detach the measurement from theoretical constraints on the operators  $\mathcal{O}(D)$ , it is convenient to fit simultaneously  $\alpha_s(M_\tau)$ ,  $\mathcal{O}(4)$ ,  $\mathcal{O}(6)$  and  $\mathcal{O}(8)$ . In order to incorporate new experimental information, we exploit the explicit shape of the (normalized) vector/axial-vector invariant mass spectrum  $(1/N_{V/A}) dN_{V/A}/ds$  by means of the spectral moments

$$D_{V/A}^{kl} = \int_0^{M_\tau^2} ds \left(1 - \frac{s}{M_\tau^2}\right)^k \left(\frac{s}{M_\tau^2}\right)^l \times \frac{1}{N_{V/A}} \frac{dN_{V/A}}{ds}, \quad (18)$$

where the choice of  $k = 1$  and  $l = 0, 1, 2, 3$  provides four additional (correlated) degrees of freedom for each vector and axial-vector fit.

#### 5.1. Theoretical Uncertainties

The estimate of theoretical uncertainties which is included in the fit takes into account uncertainties in the physical constants used and tiny contributions from quark mass corrections. In addition, the effect of unknown higher order perturbative contributions is estimated by varying the leading unknown coefficient  $K_4$  between zero and

$K_4 \approx 2|K_3(K_3/K_2)| \approx 50$  (to be compared, *e.g.*, with the experimental estimate  $K_4 = 27 \pm 5$  [44]). The effect of the unknown  $\beta_4$  coefficient of the  $\beta$ -function is estimated in a similar way but turns out to be small. The uncertainty from the ambiguity of the renormalization scale  $\mu$  is rather small; nevertheless it is considered here. We additionally include rough estimates of higher order non-perturbative operators which are not measured here that lead to small contributions to the theoretical error.

The dominant theoretical uncertainty for the prediction of  $R_{\tau,V/A}$  comes from the unknown  $K_4$  coefficient.

### Results

Computing the sum of the branching fractions from Table 1 of the exclusive contributions to the vector and axial-vector spectral function yields the semileptonic widths

$$R_{\tau,V} = 1.782 \pm 0.018 (\pm 0.016), \quad (19)$$

$$R_{\tau,A} = 1.711 \pm 0.019 (\pm 0.016), \quad (20)$$

$$R_{\tau,V+A+S} = 3.649 \pm 0.013 (\pm 0.036), \quad (21)$$

where the first errors are from experimental origin while the second ones (in parentheses) represent uncertainties in the theoretical predictions as described in Section 5.1. The value of (21) is obtained via universality from the  $\tau$  branching ratios into  $e^- \bar{\nu}_e \nu_\tau$  and  $\mu^- \bar{\nu}_\mu \nu_\tau$  and the  $\tau$  lifetime which are all taken from [11,8]. The relative rise of the theoretical error in (21) compared to (19) and (20) comes from the additional uncertainties in the strange sector. It can be reduced to  $\Delta^{\text{th}} R_{\tau,V+A+S} = 0.034$  when fitting simultaneously the mass of the strange quark via  $R_{\tau,S}$  [15].

Table 2 lists the measured values of the spectral moments (18) together with the experimental errors and the uncertainties from the theoretical predictions for the vector, axial-vector and vector plus axial-vector spectral functions. Note that all the moments obtained from the same spectral function are strongly correlated. The non-perturbative terms (17) are adjusted in the fit so that they do not contribute to the theoretical errors. In particular, theoretical uncertainties

Table 3

Fit results of  $\alpha_s(M_\tau)$  and the OPE non-perturbative contributions (17) from various input parameters: the  $V$  ( $A$ ) fit uses  $R_{\tau,V}$  ( $R_{\tau,A}$ ) and the corresponding moments. The  $(V + A)$  moments are fitted together with  $R_{\tau,V+A+S}$ . The combined fit exploits the information of  $R_{\tau,V}$ ,  $R_{\tau,A}$ ,  $R_{\tau,V+A+S}$  and  $R_{\tau,S}$  as well as the vector and axial-vector moments.

ALEPH	Vector ( $V$ )	Axial-Vector ( $A$ )	$V + A$	Combined Fit	
				Vector	Axial-Vector
$\alpha_s(M_\tau)$	$0.354 \pm 0.020$	$0.358 \pm 0.023$	$0.348 \pm 0.017$	$0.351 \pm 0.016$	
$\delta^{(4)}$	$(0.1 \pm 0.4) \times 10^{-3}$	$(-1.1 \pm 0.7) \times 10^{-3}$	$-(0.8 \pm 1.2) \times 10^{-3}$	$(-0.7 \pm 0.6) \times 10^{-3}$	
$\delta^{(6)}$	$0.029 \pm 0.004$	$-0.028 \pm 0.004$	$0.002 \pm 0.005$	$0.023 \pm 0.003$	$-0.024 \pm 0.003$
$\delta^{(8)}$	$(-9.0 \pm 1.1) \times 10^{-3}$	$(7.7 \pm 1.0) \times 10^{-3}$	$(-1.0 \pm 1.0) \times 10^{-3}$	$(-8.8 \pm 1.0) \times 10^{-3}$	$(8.3 \pm 1.0) \times 10^{-3}$
$\chi^2/\text{d.o.f.}$	0.4/1	0.4/1	0.1/1	8.0/5	

Table 2

Spectral Moments of vector ( $V$ ), axial-vector ( $A$ ) and vector plus axial-vector ( $V + A$ )  $\tau$  decay modes. The first error lines give the total experimental error including statistical and systematic uncertainties while the second error lines account for uncertainties in the theoretical prediction.

ALEPH	$l = 0$	$l = 1$	$l = 2$	$l = 3$
$D_V^{1l}$	0.7159	0.1689	0.0532	0.0227
$\Delta^{\text{exp}} D_V^{1l}$	0.0034	0.0006	0.0007	0.0006
$\Delta^{\text{th}} D_V^{1l}$	0.0037	0.0035	0.0004	0.0002
$D_A^{1l}$	0.7205	0.1471	0.0639	0.0303
$\Delta^{\text{exp}} D_A^{1l}$	0.0033	0.0009	0.0005	0.0004
$\Delta^{\text{th}} D_A^{1l}$	0.0037	0.0031	0.0005	0.0003
$D_{V+A}^{1l}$	0.7177	0.1581	0.0585	0.0265
$\Delta^{\text{exp}} D_{V+A}^{1l}$	0.0022	0.0006	0.0004	0.0004
$\Delta^{\text{th}} D_{V+A}^{1l}$	0.0037	0.0033	0.0004	0.0002

dominate the total error for the lower moments ( $l = 0, 1$ ) due to the important error contribution from the missing  $K_4$  coefficient of the perturbative expansion.

The results of the various fits of  $\alpha_s(M_\tau)$  and the non-perturbative terms of dimension  $D = 4, 6, 8$  are given in Table 3. The combined fit uses as input parameters  $R_{\tau,V}$ ,  $R_{\tau,A}$ ,  $R_{\tau,V+A+S}$ ,  $R_{\tau,S}$  and the vector and axial-vector moments. As mentioned above, the additional parameter  $R_{\tau,S} = 0.1560 \pm 0.0064$  [15] is used to adjust the

strange quark mass in order to reduce the theoretical uncertainty of the  $R_{\tau,V+A+S}$  prediction. The gain from the separation of vector and axial-vector channels compared to the inclusive  $V + A$  fit becomes obvious in the adjustment of the leading non-perturbative contributions of dimension  $D = 6$  and  $D = 8$ , which cancel in the inclusive sum. The information for their accurate determination comes mainly from the high  $l = 3, 4$  moments. Fig. 8 presents the total  $D = 6$  contribution  $\delta^{(6)} = C_6 \langle \mathcal{O}(6) \rangle / M^6$  to the vector and axial-vector hadronic widths as obtained from the combined fit. It is shown in comparison to recent experimental and theoretical constraints taken from [5,18,4,45].

Fig. 9 depicts the constraints of  $R_\tau$  and the spectral moments on  $\alpha_s(M_\tau)$  when using standard values for the non-perturbative contributions [4] with the addition of large systematic uncertainties. They are in excellent agreement with the best  $\alpha_s(M_\tau)$  measurement obtained from the combined fit. The fact that the normalization of the respective spectra ( $R_\tau$ ) and their pure shapes (spectral moments) independently give consistent results is a remarkable confirmation of the reliability of the  $\alpha_s$  measurement using  $\tau$  decays and the underlying SVZ approach (17).

The evolution [46,47] of the best  $\alpha_s(M_\tau)$ , taken from the combined fit, to the  $Z$  boson mass yields

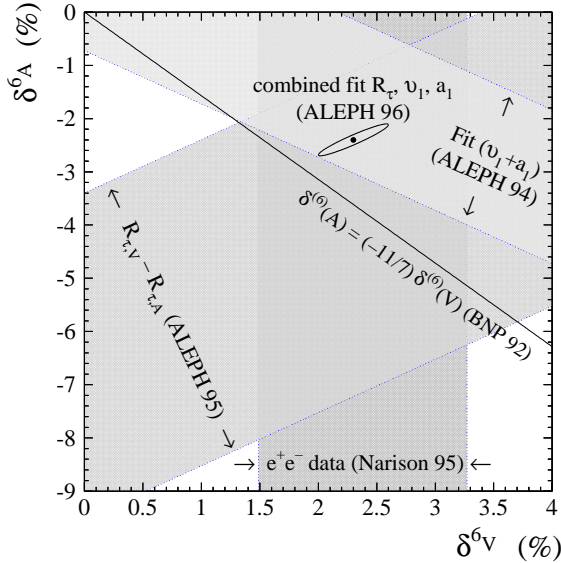


Figure 8. Non-perturbative contribution  $\delta_6$  from Eq. (17) to the  $\tau$  hadronic width of vector and axial-vector final states. The ellipse depicts the ALEPH result obtained in the combined fit.

the final result

$$\alpha_s(M_Z) = 0.1219 \pm 0.0006 \pm 0.0015 \pm 0.0010 .$$

The first error accounts for the experimental uncertainty, the second one gives the uncertainty of the theoretical prediction of  $R_\tau$  and the spectral moments, while the last error stands for possible ambiguities in the evolution due to uncertainties of the matching scales of the quark thresholds (0.0010) and effects associated with the truncation of the RGE at next-to-next-to-leading order (0.0003).

## 6. CONCLUSIONS

In this talk, we presented new results on  $\tau$  hadronic spectral functions, measured by the ALEPH Collaboration at LEP, and their implications for QCD. With small inputs from unmeasured  $\tau$  decay modes, the vector and axial-vector contributions could entirely be separated providing accurate experimental access to chiral sum rules and non-perturbative phe-

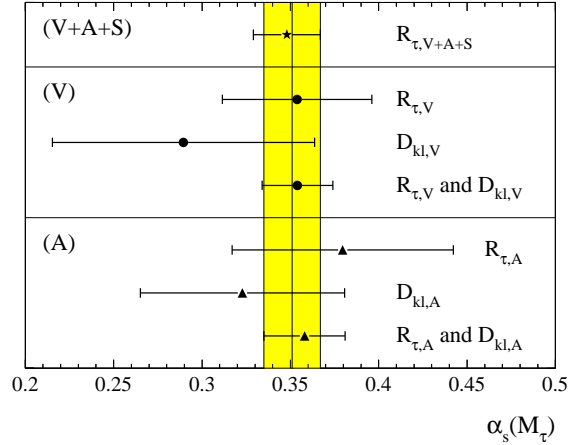


Figure 9. Results for  $\alpha_s(M_\tau)$  using  $R_\tau$  only, the moments only and the combined information from vector and axial-vector  $\tau$  decays. Additionally, the result from  $R_{\tau,V+A+S}$  only is plotted. The shaded band depicts  $\alpha_s(M_\tau)$  from the combined vector and axial-vector fit as given explicitly in Table 3.

nomenological QCD. We used moments of the Laplace-transformed Das-Mathur-Okubo (DMO) sum rule for a precise determination of the DMO integral and, through it, of the electric polarizability of the pion. Finally, we used both vector and axial-vector spectral functions for an exhaustive study of  $\alpha_s$  and leading non-perturbative terms at the  $\tau$  mass scale. For the first time, the latter could be fixed with surprising precision from  $\tau$  decays. A combined fit of all output variables yielded  $\alpha_s(M_Z) = 0.1219 \pm 0.0019$  after the evolution from the  $\tau$  to the Z mass.

## ACKNOWLEDGEMENTS

I gratefully acknowledge the organizing committee and especially J. Smith for their efforts to realize this interesting conference at such a splendid place in the Rocky Mountains. I would like to thank Michel Davier and Ricard Alemany for the fruitful collaboration during the last years of our work on  $\tau$  spectral functions.

## REFERENCES

1. R. Alemany (for the ALEPH Collaboration), ‘Measurement of the Spectral functions of Vector Current Hadronic  $\tau$  decays’, Talk given at the TAU96 Conference, Colorado, 1996.
2. D. Buskulic *et al.* (ALEPH Collaboration), *to be published*.
3. M.A. Shifman, A.L. Vainshtein and V.I. Zakharov, *Nucl. Phys.* **B147** (1979) 385, 448, 519.
4. E. Braaten, S. Narison and A. Pich, *Nucl. Phys.* **B373** (1992) 581.
5. D. Buskulic *et al.* (ALEPH Collaboration), *Phys. Lett.* **B307** (1993) 209.
6. L. Duf/lot, *Nucl. Phys.* **B40** (Proc. Suppl.) (1995) 37.
7. T. Coan *et al.* (CLEO Collaboration), *Phys. Lett.* **B356** (1995) 580.
8. R.M. Barnett *et al.* (Particle Data Group), *Phys. Rev.* **D54** (1996) 1.
9. W.J. Marciano and A. Sirlin, *Phys. Rev. Lett.* **56** (1986) 22.
10. J.Z. Bai *et al.* (BES Collaboration), *Phys. Rev.* **D53** (1996) 20.
11. P. Weber, ‘Review of  $\tau$  lifetime measurements’, Talk given at the TAU96 Conference, Colorado, 1996.
12. J.F. Donoghue and E. Golowich, *Phys. Rev.* **D49** (1994) 1513.
13. A. Pich, *Nucl. Phys.* **B39** (Proc. Suppl.) (1995) 326.
14. D. Decamp *et al.* (ALEPH Collaboration), *Nucl. Inst. Meth.* **A294** (1990) 121; D. Buskulic *et al.* (ALEPH Collaboration), *Nucl. Inst. Meth.* **A360** (1995) 481.
15. M. Davier, ‘ $\tau$  decays into strange particles and QCD’, Talk given at the TAU96 Conference, Colorado, 1996.
16. D. Buskulic *et al.* (ALEPH Collaboration), *Z. Phys.* **C62** (1994) 539.
17. D. Buskulic *et al.* (ALEPH Collaboration), *Z. Phys.* **C70** (1996) 561.
18. D. Buskulic *et al.* (ALEPH Collaboration), *Z. Phys.* **C70** (1996) 579.
19. D. Decamp *et al.* (ALEPH Collaboration), *Z. Phys.* **C54** (1992) 211.
20. A. Höcker and V. Kartvelishvili, *Nucl. Inst. Meth.* **A372** (1996) 469.
21. A. Rougé (for the ALEPH Collaboration), ‘Tau decays involving  $\eta$  and  $\omega$  mesons’, Talk given at the TAU96 Conference, Colorado, 1996.
22. V. Shelkov (for the CLEO Collaboration), ‘Tau decays involving  $\eta$  mesons and  $\tau^- \rightarrow f_1 \pi \nu_\tau$ ’, Talk given at the TAU96 Conference, Colorado, 1996.
23. P.L. Campana (for the ALEPH Collaboration), ‘Branching fractions for modes involving kaons’, Talk given at the TAU96 Conference, Colorado, 1996.
24. S. Jadach, J.H. Kühn and Z. Wąs, *Comp. Phys. Comm.* **64** (1991) 275; S. Jadach, B.F.L. Ward and Z. Wąs, *Comp. Phys. Comm.* **79** (1994) 503; S. Jadach *et al.*, *Comp. Phys. Comm.* **76** (1993) 361.
25. A. Rougé, *Z. Phys.* **C70** (1996) 65.
26. A. Pais, *Ann. Phys.* **9** (1960) 548.
27. T. Das, V.S. Mathur and S. Okubo, *Phys. Rev. Lett.* **19** (1967) 895.
28. S.R. Amendolia *et al.* (NA7 Collaboration), *Nucl. Phys.* **B277** (1986) 168.
29. G. Coangelo, M. Finkemeier and R. Urech, ‘Tau Decays and Chiral Perturbation Theory’, *Preprint BUTP-96/9 HUTP95/-A051, TTP96-02, hep-ph/9604279* (1996).
30. S. Weinberg, *Phys. Rev. Lett.* **18** (1967) 507.
31. E.G. Floratos, S. Narison and E. de Rafael, *Nucl. Phys.* **B155** (1979) 115; R.d. Peccei and J. Solà, *Nucl. Phys.* **B281** (1987) 1.
32. T. Das, G.S. Guralnik, V.S. Mathur, F.E. Low and J.E. Young, *Phys. Rev. Lett.* **18** (1967) 759.
33. M.V. Terent’ev, *Sov. J. Nucl. Phys.* **16** (1973) 87; B.R. Holstein, *Comm. Nucl. Part. Phys.* **19** (1990) 221.
34. V. Kartvelishvili, M. Margvelashvili and G. Shaw, ‘Pion Polarisability and Hadronic  $\tau$  Decays’, Talk given at the QCD96 Conference, Montpellier, 1996.
35. L.E. Pilonen *et al.*, *Phys. Rev. Lett.* **57** 1402; A. Bay *et al.*, *Phys. Lett.* **B174** (1986) 445; V.N. Bolotov *et al.*, **B243** (1990) 308.
36. D.A. Bryman *et al.*, *Phys. Rep.* **88** (1982) 151.
37. V. Kartvelishvili, *Phys. Lett.* **B287** (1992)

- 159; V. Kartvelishvili and M. Margvelashvili, *Z. Phys.* **C55** (1992) 83.
38. M.V. Margvelashvili, *Phys. Lett.* **B215** (1988) 763.
39. F. Le Diberder and A. Pich, *Phys. Lett.* **B289** (1992) 165;
40. F. Le Diberder and A. Pich, *Phys. Lett.* **B286** (1992) 147;
41. S. Narison, *Nucl. Phys.* **B40** (Proc. Suppl.) (1995) 47; G. Altarelli, P. Nason and G. Ridolfi, *Z. Phys.* **C68** (1995) 257; M. Neubert, *Nucl. Phys.* **B463** (1996) 511; P.A. Rączka and A. Szymacha, *Z. Phys.* **C70** (1996) 125.
42. S. Narison and A. Pich, *Phys. Lett.* **B211** (1988) 183.
43. E. Braaten and C.S. Li, *Phys. Rev.* **D42** (1990) 3888.
44. F. Le Diberder, *Nucl. Phys.* **B39** (Proc. Suppl.) (1995) 318.
45. S. Narison, *Phys. Lett.* **B361** (1995) 121;
46. W. Bernreuther and W. Wetzel, *Nucl. Phys.* **B197** (1982) 228.
47. W. Bernreuther, Workshop 'QCD at LEP', Aachen, 1994.